SOLAR CELLS

Amidination of ligands for chemical and field-effect passivation stabilizes perovskite solar cells

Yi Yang[1]†, Hao Chen[1]†, Cheng Liu[1]†, Jian Xu[2]†, Chuying Huang[1], Christos D. Malliakas[1], Haoyue Wan[1,2], Abdulaziz S. R. Bati[1], Zaiwei Wang[2], Robert P. Reynolds[1], Isaiah W. Gilley[1], Shuta Kitade[1], Taylor E. Wiggins[1], Stefan Zeiske[1], Selengesuren Suragtkhuu[3], Munkhbayar Batmunkh[3], Lin X. Chen[1,4], Bin Chen[1]*, Mercouri G. Kanatzidis[1]*, Edward H. Sargent[1,2,5]*

Surface passivation has driven the rapid increase in the power conversion efficiency (PCE) of perovskite solar cells (PSCs). However, state-of-the-art surface passivation techniques rely on ammonium ligands that suffer deprotonation under light and thermal stress. We developed a library of amidinium ligands, of interest for their resonance effect–enhanced N–H bonds that may resist deprotonation, to increase the thermal stability of passivation layers on perovskite surfaces. This strategy resulted in a >10-fold reduction in the ligand deprotonation equilibrium constant and a twofold increase in the maintenance of photoluminescence quantum yield after aging at 85°C under illumination in air. Implementing this approach, we achieved a certified quasi–steady-state PCE of 26.3% for inverted PSCs; and we report retention of ≥90% PCE after 1100 hours of continuous 1-sun maximum power point operation at 85°C.

P erovskite solar cells (PSCs) have rapidly developed in the past 2 years, achieving certified stabilized power conversion efficiencies (PCEs) of >26% (*1*). A key factor driving this advancement is the implementation of surface passivation techniques, including the use of low-dimensional perovskites, aromatic amines, and ammonium ligands (*2–6*).

State-of-the-art PSCs use organic ammonium ligands to address surface defects and reduce nonradiative recombination at the perovskite–charge transport layer interface, enabled by the ammonium functional groups' strong electrostatic interactions with charged surface defects, as well as their tunable chemical properties (*1, 7–9*). While distinct classes of ammonium ligands enable chemical and field-effect pas-

sivation (*6*), ammonium ligands also tend to deprotonate into volatile amines and halogens, especially under light and thermal stress (*10–13*). The amines can react with perovskite through a transimination reaction (*2, 14, 15*). Ammonium deprotonation leads to the loss of passivation efficacy and creates vacancy defects at the perovskite film surface over the course of extended device operation (*14*). As a result, these highest-efficiency (≥25%) PSCs exhibit limited operating stability, with a T_{80} (the duration for the device efficiency to decay to 80% of the initial value) of ~500 hours at maximum power point (MPP) tracking under 85°C in a 50% relative humidity (RH) environment, also known as ISOS-L-3-85°C protocol (ISOS: International Summit on Organic Photovoltaic Stability) (*1, 16*).

During the development of methods to improve perovskite stability, it was found that amidinium [–C(NH₂)₂⁺] cations offer greater

[1]Department of Chemistry, Northwestern University, Evanston, IL, USA. [2]Department of Electrical and Computer Engineering, University of Toronto, Toronto, ON, Canada. [3]Queensland Micro- and Nanotechnology Centre, School of Environment and Science, Griffith University, Nathan, QLD, Australia. [4]Chemical Science and Engineering Division, Argonne National Laboratory, Lemont, IL, USA. [5]Department of Electrical and Computer Engineering, Northwestern University, Evanston, IL, USA.
*Corresponding author. Email: bin.chen@northwestern.edu (B.C.); m-kanatzidis@northwestern.edu (M.G.K.); ted.sargent@northwestern.edu (E.H.S.)
†These authors contributed equally to this work.
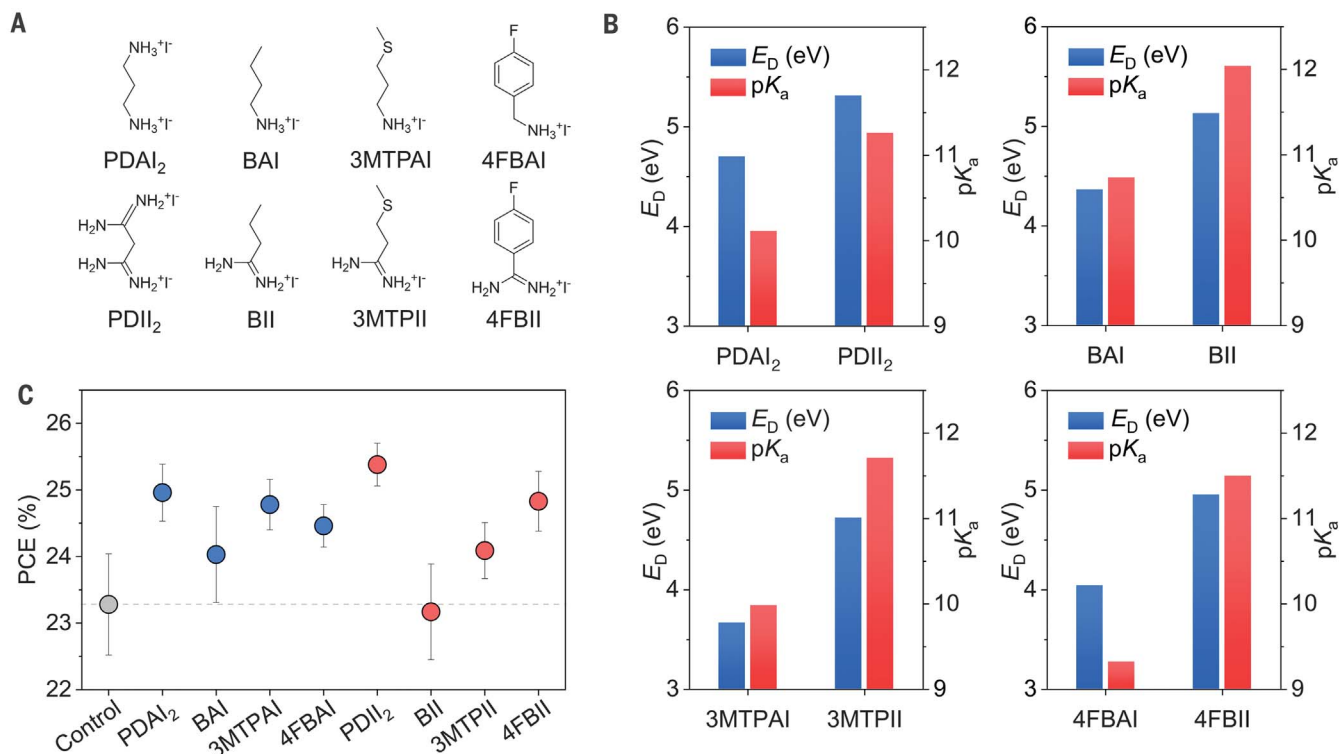
Fig. 1. Stability of amidinium ligands. (**A**) Molecular structures of ligands used in this study. (**B**) The N–H dissociation energies (E_D) of ammonium ligands and their corresponding amidinium ligands obtained by DFT calculations and acid dissociation constant (pK_a) values measured by titration of a 0.05 N ligand solution with 0.05 N NaOH. (**C**) PCE comparison of PSCs using different ligand passivation. Twelve devices were evaluated at each condition, and data are presented as mean ± standard deviation.

structural and thermal stability than do ammonium cations. The ammonium group adopts a tetrahedral geometry with three hydrogen atoms and an alkyl or aryl group; that is, it forms three hydrogen bonds with halide ions. In contrast, the amidinium group has a planar structure and can form four hydrogen bonds with halides, the result of its higher number of hydrogen atoms. The amidinium cations benefit from resonance stabilization, where the positive charge is delocalized along the N–C–N backbone across multiple atoms, reducing overall energy and making these more stable than the localized positive charge on ammonium cations (*17, 18*). Substituting methylammonium (MA) with formamidinium (FA) in the perovskite bulk increases the formation energy of hydrogen vacancies and impedes the deprotonation of ligands, thereby enhancing the stability of perovskite materials (*19–23*). Amidinium ligands such as phenylamidinium and 2-amidinopyridine have been shown to provide passivation (*24, 25*).

Thus, the stability of amidinium-based passivators remains a topic warranting study. It is important—in order to maximize the open-circuit voltage (V_{OC})—to provide not only chemical passivation but also field-effect passivation, yet field-effect passivators based on amidinium compounds have yet to be investigated in depth.

We hypothesized that changing the head group from ammonium to amidinium in both chemical and field-effect passivators could address deprotonation-induced instability of each class of molecules at elevated temperatures, thus potentially improving the operating stability of PSCs and doing so without sacrificing efficiency.
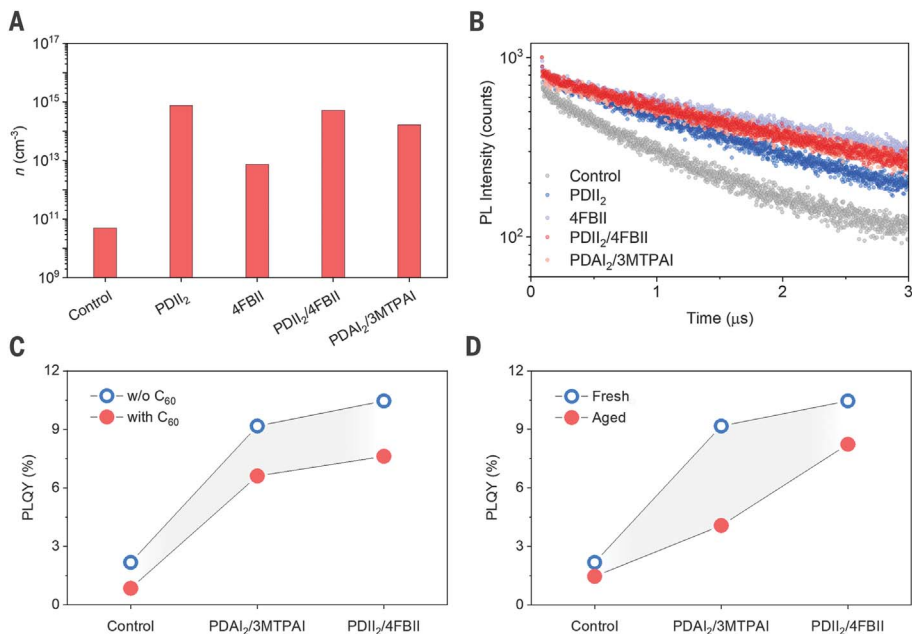
Stability of amidinium ligands

We used density functional theory (DFT) to examine the effect of amidation on ammonium ligand deprotonation ability (Fig. 1, A and B, and fig. S1). For commonly used field-effect and chemical passivators, such as propane-1,3-diammonium iodide (PDAI$_2$), butylammonium iodide (BAI), 3-(methylthio)propylammonium iodide (3MTPAI), and 4-fluorobenzylammonium iodide (4FBAI) (*6, 26–29*), incorporation of amidinium as head groups resulted in new passivators, namely propanediimidamide hydroiodide (PDII$_2$), butanimidamide hydroiodide (BII), 3-(methylthio)propanimidamide hydroiodide (3MTPII), and 4-fluorobenzimidamide hydroiodide (4FBII), for which the N–H bond dissociation energies (E_D) increased by 13, 18, 29, and 23%, respectively. We also experimentally assessed the ligand deprotonation capacity using the titration method, seeking to determine the acid dissociation constant (pK_a). As shown in Fig. 1B, amidinium cations exhibited pK_a values at least 10% higher than those of their ammonium counterparts, corresponding to a >90% decrease in the deprotonation equilibrium constant (K_a), indicating suppression of the deprotonation process. Among these, PDII$_2$ and 4FBII exhibited superior surface passivation effects in PSCs with the architecture of fluorine-doped tin oxide (FTO)/self-assembled monolayers (SAMs)/perovskite/passivation layer/C$_{60}$/SnO$_x$/Cu (Fig. 1C).

We analyzed ligand deprotonation by heating the ligand powders under airflow and using a combined system of mass spectrometry (MS)
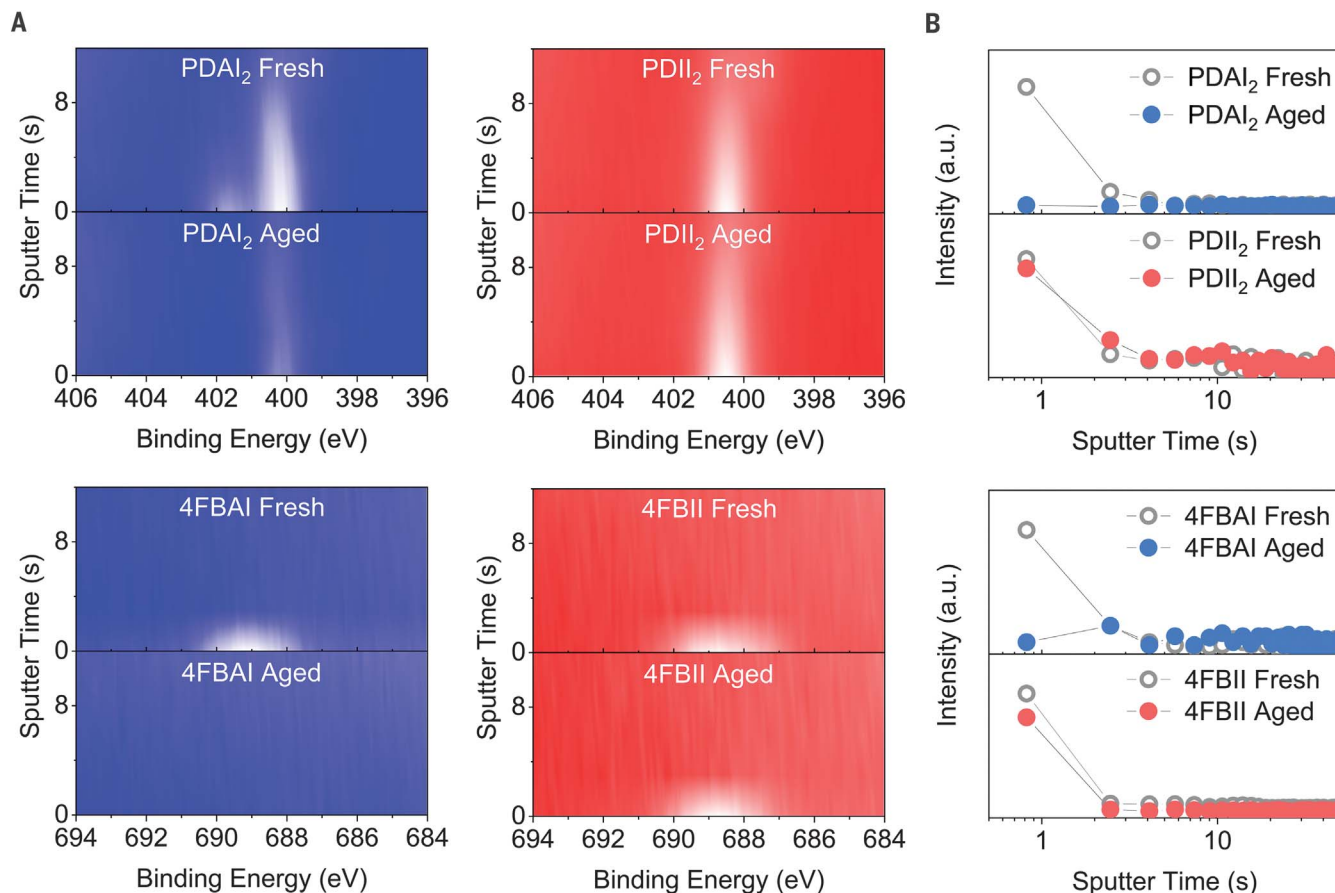
Fig. 2. Stability of amidinium passivation layers. (**A**) N 1s XPS depth profile of fresh and aged perovskite films treated with PDAI$_2$ and PDII$_2$, and F 1s depth profile of fresh and aged perovskite films treated with 4FBAI and 4FBII. The white color represents the highest intensity, while the red and blue represent the lowest intensity. (**B**) ToF-SIMS of C$_3$H$_{12}$N$_2^{2+}$, C$_7$H$_9$FN$^+$, C$_3$H$_{10}$N$_4^{2+}$, and C$_7$H$_8$FN$_2^+$ for fresh and aged perovskite films treated with PDAI$_2$, PDII$_2$, 4FBAI, and 4FBII, respectively. a.u., arbitrary units.

Fig. 3. Passivation effect of amidinium ligands. (**A**) The electron density in the conduction band (n) near the surface of perovskite films with different treatments. (**B**) TRPL spectra of perovskite films with different treatments. (**C**) PLQY of the control, PDAI$_2$/3MTPAI-based, and PDII$_2$/4FBII-based perovskite films with and without C$_{60}$ deposition. (**D**) PLQY of the control, PDAI$_2$/3MTPAI-based, and PDII$_2$/4FBII-based perovskite films without C$_{60}$ before and after aging under 85°C, 1-sun-equivalent light illumination, and 50% RH in air.

coupled with thermogravimetric analysis (TGA) to detect volatile deprotonation products. Evaporation of I$_2$, which we attributed to the oxidation reaction of generated hydrogen iodide (HI) under high temperature (*30*), was observed for ammonium ligands (PDAI$_2$ and 4FBAI; fig. S2) but not for their corresponding amidinium ligands, PDII$_2$ and 4FBII. Amidination of head groups suppressed ligand deprotonation at elevated temperatures.

Stability of amidinium passivation layers

We deposited ligands on the perovskite surface by dynamically spin-coating isopropanol solutions onto perovskite films. Scanning electron microscopy (SEM) images showed a loss of surface terracing after ligand deposition, a feature of isopropanol-washed films (fig. S3). X-ray diffraction (XRD) showed an absence of observable low-dimensional perovskite after ligand treatment (fig. S4).

To evaluate the stability of the ligand passivation layers, we exposed the treated perovskite films to accelerated conditions of 85°C, 1-sun-equivalent light illumination, and 50% RH in air for 2 hours. X-ray photoelectron spectroscopy (XPS) depth profiling showed that the characteristic N 1s peak of PDAI$_2$ at 401.7 eV disappeared after aging (Fig. 2A), whereas the other N 1s peak at 400.2 eV, which overlaps with that of the perovskite, showed decreased surface-to-bulk counts in the aged film. Similarly, the disappearance of the characteristic

peak of F 1s at 689.0 eV was observed for 4FBAI-treated perovskite film after aging. These changes indicated a loss of ammonium ligands on the perovskite surface, accelerated in the presence of moisture. In contrast, films treated with the amidinium ligands PDII$_2$ and 4FBII showed little change in their characteristic elemental peaks, consistent with the view that the use of amidinium ligands led to more-stable passivation of the top surface of perovskite films. This we connect to their higher resistance to deprotonation, evidenced by their higher pK_a values (Fig. 1B).

Time-of-flight secondary ion mass spectrometry (ToF-SIMS) further confirmed the ammonium ligand loss on the perovskite surface during aging. As shown in Fig. 2B and fig. S5, we observed 99 and 85% losses in the initial signal of C$_3$H$_{12}$N$_2$$^{2+}$ and C$_7$H$_9$FN$^+$ on the film surfaces for PDAI$_2$- and 4FBAI-treated perovskite films, respectively. No cation migration was observed, so we attributed these signal losses to the deprotonation behavior of the ammonium ligands. Perovskite films treated with PDII$_2$ and 4FBII maintained 93 and 80% of their initial signal of C$_3$H$_{10}$N$_4$$^{2+}$ and C$_7$H$_8$FN$_2$$^+$, respectively, which is attributed to their higher deprotonation resistance.

Amidinium bimolecule passivation

Bimolecular passivation, in which two molecules provide field-effect and chemical passivation, respectively, such as the PDAI$_2$/3MTPAI combination, can repel hole carriers and interact

with defect sites to form chemical bonds, thereby reducing complex carrier recombination at the perovskite–electron transport layer (ETL) interface (*6*). Instead of ammonium bimolecular passivation (ABP), we attempted to develop amidinium bimolecular passivation (ADBP) to achieve both comprehensive passivation and improved stability of the passivation layers.

We used ultraviolet photoelectron spectroscopy (UPS) to study the effect of these amidinium ligands and the ADBP strategy on the band-edge energies of perovskite. The energy level difference between the conduction band minimum and the Fermi level was used to assess the electron density in the conduction band (n) near the perovskite surface (Fig. 3A and figs. S6 and S7) (*31*). The electron density increased to 8×10^{14} cm^{-3} after PDII$_2$ treatment compared with 5×10^{10} cm^{-3} and 8×10^{12} cm^{-3} for control (without treatment) and 4FBII treatment, respectively, which is indicative of field-effect passivation by PDII. We attributed the improved n-type doping effect of PDII$_2$ to its additional amidinium group, which induced a surface dipole that repelled minority carriers at the interface, similar to the effects observed with ethane-1,2-diammonium iodide (EDAI$_2$) and PDAI$_2$ (*32*, *33*). When the ADBP strategy was implemented with the PDII$_2$/4FBII (5.2×10^{14} cm^{-3}) combination, n-type doping was also observed, comparable to the ABP method with the PDAI$_2$/3MTPAI combination (1.7×10^{14} cm^{-3}).

Time-resolved photoluminescence (TRPL) measurements were used to evaluate the chemical passivation effect (Fig. 3B). Among the amidinium ligands, 4FBII treatment enabled the longest carrier lifetime (2.6 µs), compared with 1.6 µs for PDII$_2$. We attributed suppression of defect-induced nonradiative carrier recombination on the perovskite surface to chemical interactions between the ligands and the perovskite surface, as seen in XPS (fig. S8). The PDII$_2$/4FBII treatment also showed a notably increased carrier lifetime of 2.4 µs, compared with 1.0 µs of the control film; thus, the chemical passivation effect offered by 4FBII is retained in the case of the ADBP strategy.

To probe the overall surface and interface recombination and access the durability of different bimolecular passivation strategies, we measured the photoluminescence quantum yield (PLQY) of partial and full perovskite–ETL device stacks before and after accelerated aging. After bimolecular treatments with PDAI$_2$/3MTPAI and PDII$_2$/4FBII (Fig. 3C), the perovskite films exhibited a more than threefold increase in PLQY and retained >70% of their initial PLQY after C$_{60}$ deposition, indicating the combined field-effect and chemical passivation. However, the PDAI$_2$/3MTPAI-treated film retained <40% PLQY regardless of the C$_{60}$ coverage after 2 hours of aging under 85°C, 1-sun-equivalent light illumination, and 50% RH in air (Fig. 3D and fig. S9). In contrast, ADBP-based films treated with
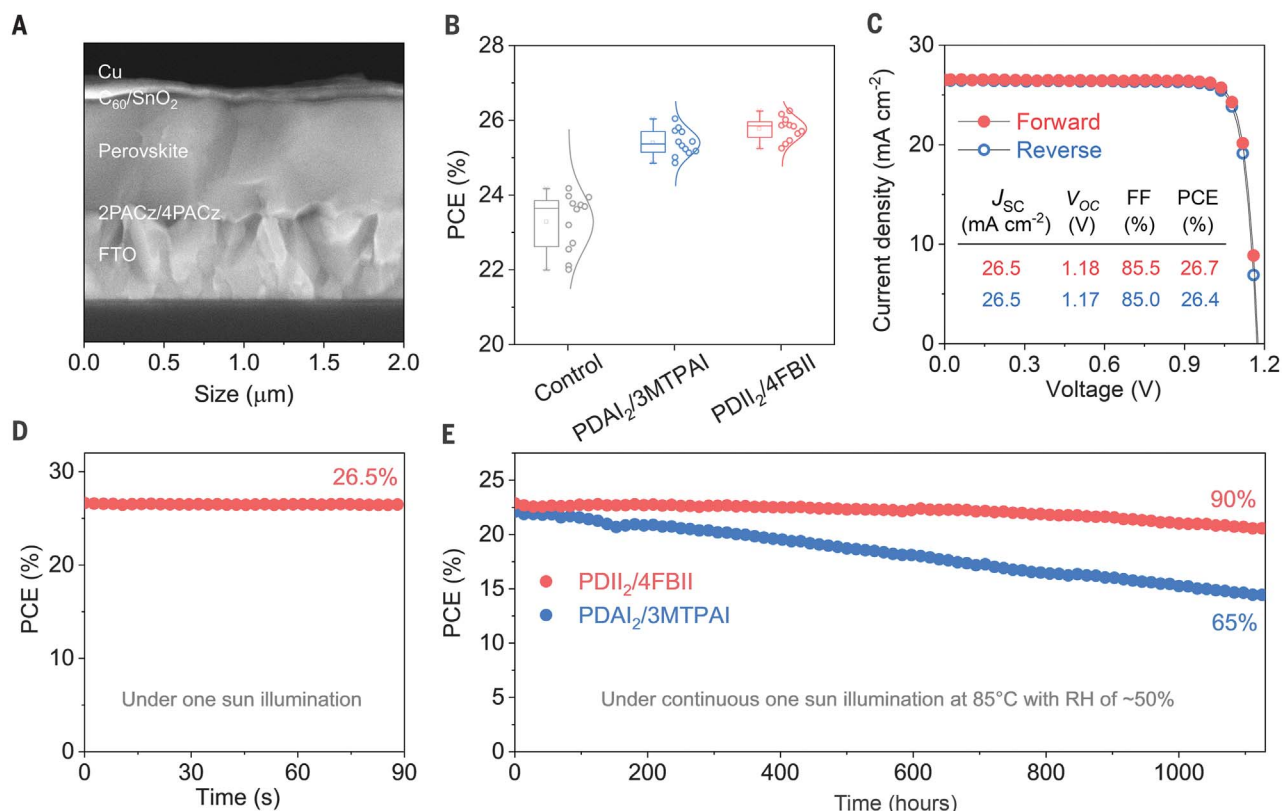
Fig. 4. Device performance. (**A**) Cross-sectional SEM image of the device structure. (**B**) PCE statistics for control, PDAI$_2$/3MTPAI-passivated, and PDII$_2$/4FBII-passivated devices. The center line indicates the median, the box limits represent the upper and lower quartiles, the whiskers denote the minimum and maximum values, and the vertical curved lines illustrate the data distribution. (**C**) Current density–voltage (*J-V*) curves of the best PDII$_2$/4FBII-passivated device. (**D**) The stabilized power output of the PDII$_2$/4FBII-passivated device. (**E**) MPP stability tracking of glass-encapsulated devices under 1-sun illumination at 85°C under 50% RH in air.

PDII$_2$/4FBII showed enhanced PLQY retention, maintaining ~70% of their initial value after aging, which we attributed to the suppressed deportation of the amidinium ligands.

Inverted PSCs

Using the ADBP strategy, we fabricated inverted PSCs (Fig. 4A). Device statistics (Fig. 4B) indicated a substantial enhancement in average PCE for the devices passivated with PDII$_2$/4FBII, achieving 25.9%, compared with 23.7% for the control devices, primarily from increased V_{OC} and fill factor (FF). Devices treated with PDAI$_2$/3MTPAI showed a comparable average PCE of 25.4%. Device performance based on single amidinium passivation is also summarized in fig. S10.

The best-performing PDII$_2$/4FBII-based device, with an active area of 0.05 cm^2, achieved a PCE of 26.7%, a short-circuit current density (J_{SC}) of 26.5 mA cm^{-2}, a V_{OC} of 1.18 V, and an FF of 85.5% (Fig. 4C), along with a steady-state PCE of 26.5% (Fig. 4D). The large device, with an active area of 1.04 cm^2, achieved a PCE of 25% (fig. S11). The external quantum efficiency (EQE) spectrum indicated a bandgap of 1.53 eV for the device (fig. S12). We sent devices to an independent photovoltaic calibration laboratory [National Photovoltaic Industry Measurement

and Testing Center (NPVM)] for certification and achieved a certified stabilized PCE of 26.3% (fig. S13).

We sought to understand how the ADBP strategy affected the operating stability of PSCs. Accelerated lifetime testing was conducted on encapsulated devices under the ISOS-L-3 protocol, which involved light-soaking at 85°C and 50% RH, along with MPP tracking (fig. S14). The PDII$_2$/4FBII-based PSC achieved a T_{90} (the duration for the device efficiency to decay to 90% of the initial value) of 1130 hours, whereas the PDAI$_2$/3MTPAI-based PSC lost 35% of its initial efficiency over the same period (Fig. 4E). These results represent the best combination of PCE and operating stability under elevated temperature conditions (table S1) (*1, 6, 34*).

Discussion

Changing the anchoring group of the passivation ligands from ammonium to amidinium impedes the ligand deprotonation and extends the stability of the passivation layer at elevated temperatures while maintaining the passivation efficacy. We consider the amidination of ligands, combined with expanded functionalities, a promising direction for developing next-generation passivation strategies to enhance the durability of efficient perovskite optoelectronics.

REFERENCES AND NOTES

1. H. Chen *et al.*, *Science* **384**, 189–193 (2024).
2. Q. Jiang *et al.*, *Nature* **611**, 278–283 (2022).
3. S. You *et al.*, *Nat. Energy* **8**, 515–525 (2023).
4. R. Azmi *et al.*, *Nature* **628**, 93–98 (2024).
5. S. Sidhik *et al.*, *Science* **377**, 1425–1430 (2022).
6. C. Liu *et al.*, *Science* **382**, 810–815 (2023).
7. S. Akin *et al.*, *Adv. Sci. (Weinh.)* **8**, 2004593 (2021).
8. C. Liu *et al.*, *Nat. Commun.* **12**, 6394 (2021).
9. C. Liu *et al.*, *Nature* **633**, 359–364 (2024).
10. M. Li *et al.*, *Angew. Chem. Int. Ed.* **61**, e202206914 (2022).
11. H. Meng *et al.*, *Nat. Energy* **9**, 536–547 (2024).
12. J. Zhuang, J. Wang, F. Yan, *Nano-Micro Lett.* **15**, 84 (2023).
13. M. Wang *et al.*, *Nat. Energy* **8**, 1229–1239 (2023).
14. Z. Li *et al.*, *Nat. Commun.* **13**, 4417 (2022).
15. M. Taddei *et al.*, *ACS Energy Lett.* **7**, 4265–4273 (2022).
16. M. V. Khenkin *et al.*, *Nat. Energy* **5**, 35–49 (2020).
17. K. Schutt *et al.*, *Adv. Funct. Mater.* **29**, 1900466 (2019).
18. C. C. Boyd, R. Cheacharoen, T. Leijtens, M. D. McGehee, *Chem. Rev.* **119**, 3418–3451 (2019).
19. X. Zhang, J.-X. Shen, M. E. Turiansky, C. G. Van de Walle, *Nat. Mater.* **20**, 971–976 (2021).
20. T. A. S. Doherty *et al.*, *Science* **374**, 1598–1605 (2021).
21. Z. Zheng *et al.*, *Chem. Sci.* **13**, 2167–2183 (2022).
22. Y. Liu *et al.*, *Angew. Chem. Int. Ed.* **59**, 15688–15694 (2020).
23. S. Sidhik *et al.*, *Science* **384**, 1227–1235 (2024).
24. C. Ma *et al.*, *J. Am. Chem. Soc.* **145**, 24349–24357 (2023).
25. J.-H. Kim, D.-H. Kang, D.-N. Lee, N.-G. Park, *J. Mater. Chem. A* **11**, 15014–15021 (2023).
26. J. Hu *et al.*, *Nat. Commun.* **10**, 1276 (2019).
27. F. Zhang *et al.*, *J. Am. Chem. Soc.* **141**, 5972–5979 (2019).
28. Z. Liu *et al.*, *Adv. Mater.* **36**, 2308370 (2024).
29. A. R. Mohd Yusoff *et al.*, *Energy Environ. Sci.* **14**, 2906–2953 (2021).

30. Y. Han *et al.*, *J. Mater. Chem. A* **3**, 8139–8147 (2015).
31. Y. Zhou, G. Long, *J. Phys. Chem. C* **121**, 1455–1462 (2017).
32. C. Quarti, F. De Angelis, D. Beljonne, *Chem. Mater.* **29**, 958–968 (2017).
33. S. Hu *et al.*, *Energy Environ. Sci.* **15**, 2096–2107 (2022).
34. S. M. Park *et al.*, *Science* **381**, 209–215 (2023).

SUPPLEMENTARY MATERIALS

science.org/doi/10.1126/science.adr2091
Materials and Methods
Figs. S1 to S14
Table S1
Reference (*35*)

Submitted 21 June 2024; accepted 15 October 2024
10.1126/science.adr2091